

ORIGINAL ARTICLE

## Nitro-Oleic Acid (NO<sub>2</sub>-OA) Release Enhances Regional Angiogenesis in a Rat Abdominal Wall Defect Model

Antonio D'Amore, PhD,<sup>1-3</sup> Marco Fazzari, PhD,<sup>2,4</sup> Hong-Bin Jiang, MD,<sup>1</sup> Samuel K. Luketich, BS,<sup>5</sup> Michael E. Luketich,<sup>5</sup> Richard Hoff, MA,<sup>1</sup> Daniel L. Jacobs,<sup>1</sup> Xinzhu Gu, PhD,<sup>1</sup> Stephen F. Badylak, DVM, PhD, MD,<sup>1</sup> Bruce A. Freeman, PhD,<sup>4</sup> and William R. Wagner, PhD<sup>1,5</sup>

Ventral hernia is often addressed surgically by the placement of prosthetic materials, either synthetic or from allogeneic and xenogeneic biologic sources. Despite advances in surgical approaches and device design, a number of postsurgical limitations remain, including hernia recurrence, mesh encapsulation, and reduced vascularity of the implanted volume. The *in situ* controlled release of angiogenic factors from a scaffold facilitating abdominal wall repair might address some of these issues associated with suboptimal tissue reconstruction. Furthermore, a biocomposite material that combines the favorable mechanical properties achievable with synthetic materials and the bioactivity associated with xenogeneic tissue sources would be desirable. In this report, an abdominal wall repair scaffold has been designed based on a microfibrillar, elastomeric poly(ester carbonate)urethane urea matrix integrated with a hydrogel derived from decellularized porcine dermis (extracellular matrix [ECM] gel) and poly(lactic-co-glycolic acid) (PLGA) microspheres loaded with nitro-oleic acid (NO<sub>2</sub>-OA). NO<sub>2</sub>-OA is an electrophilic fatty acid nitro-alkene derivative that, under hypoxic conditions, induces angiogenesis. This scaffold was utilized to repair a rat abdominal wall partial thickness defect, hypothesizing that the nitro-fatty acid release would facilitate increased angiogenesis at the 8-week endpoint. The quantification of neovascularization was conducted by novel methodologies to assess vessel morphology and spatial distribution. The repaired abdominal wall defects were evaluated by histopathologic methods, including quantification of the foreign body response and cellular ingrowth. The results showed that NO<sub>2</sub>-OA release was associated with significantly improved regional angiogenesis. The combined biohybrid scaffold and NO<sub>2</sub>-OA-controlled release strategy also reduced scaffold encapsulation, increased wall thickness, and enhanced cellular infiltration. More broadly, the three components of the composite scaffold design (ECM gel, polymeric fibers, and PLGA microparticles) enable the tuning of performance characteristics, including scaffold bioactivity, degradation, mechanics, and drug release profile, all decisive factors to better address current limitations in abdominal wall repair or other soft tissue augmentation procedures.

**Keywords:** angiogenesis, abdominal wall defect model, nitro-oleic acid, elastomeric patch, dermal ECM

### Introduction

VENTRAL HERNIA is one of the most common complications following abdominal surgery. In 2004, more than 1000 patients died with abdominal wall hernia as the underlying cause. The definitive treatment remains surgical repair. With ~800,000 hernia repairs<sup>1</sup> performed annually

in the United States, this tissue insufficiency creates a consistent healthcare burden and substantially impacts the quality of life for those patients affected.<sup>2,3</sup>

Prosthetic surgical mesh materials, either synthetic or from allogeneic and xenogeneic sources, have been shown to decrease the incidence of hernia recurrence compared to direct tissue apposition. Improved surgical<sup>4,5</sup> and device<sup>6,7</sup>

<sup>1</sup>Departments of Bioengineering and Surgery, McGowan Institute for Regenerative Medicine, University of Pittsburgh, Pittsburgh, Pennsylvania.

<sup>2</sup>Fondazione RiMED, Palermo, Italy.

<sup>3</sup>Dipartimento Innovazione Industriale e Digitale (DIID), Università di Palermo, Palermo, Italy.

Departments of <sup>4</sup>Pharmacology and Chemical Biology and <sup>5</sup>Chemical Engineering, University of Pittsburgh, Pittsburgh, Pennsylvania.

approaches have reduced the impact of typical complications such as chronic patient discomfort, surgical site infections, and fistulas. Despite these advances, a number of issues remain, including a high incidence of hernia recurrence, encapsulation of mesh materials, incomplete tissue remodeling, mechanical mismatch at the native tissue-implant interface, and reduced vascularity at the surgical site.<sup>8</sup>

These limitations have encouraged regenerative medicine/tissue engineering approaches, where synthetic meshes combined with cells or biologic materials are designed to function as temporary tissue surrogates and intended to be gradually replaced or remodeled by host tissue.

Previous experiences with elastic biodegradable synthetic materials<sup>9</sup> such as poly(ester carbonate)urethane urea (PECUU)<sup>10</sup> combined with dermal extracellular matrix (ECM) hydrogels have demonstrated the capacity to improve cellular infiltration, reduce native tissue-prosthesis mechanical mismatch, and facilitate tissue remodeling.<sup>8</sup> Despite these advancements in devices that promote constructive tissue remodeling, the level of muscle function and vascularity observed typically does not match that of the native healthy abdominal wall. Toward this end, the *in situ* controlled release of angiogenic factors might improve the outcomes when such materials are used for the reconstruction of the diseased abdominal wall or for a variety of other applications, such as cardiovascular tissue repair and augmentation.<sup>11</sup>

Electrophilic fatty acid nitro-alkene derivatives (nitro-fatty acids, NO<sub>2</sub>-FA) are endogenously generated by pro-oxidative inflammatory reactions and the acidic gastric milieu during digestion.<sup>12–14</sup> The electrophilic nature of NO<sub>2</sub>-FA induces reversible posttranslational modification of cysteine-containing proteins, many regulating metabolic and inflammatory signaling, cell signaling, and gene expression responses.<sup>15–19</sup> The beneficial and anti-inflammatory effects of NO<sub>2</sub>-FA have been shown in various animal models of disease<sup>20</sup> and soon nitrooleic acid (NO<sub>2</sub>-OA) is entering U.S. Food and Drug Administration (FDA) phase II clinical trials for the treatment of chronic renal and pulmonary diseases.

Notably, NO<sub>2</sub>-FA induces both endothelial nitric oxide synthase gene and protein expression (Kuo Free Radical Biology & Medicine) and promotes angiogenesis through an NO-dependent activation of hypoxia-inducible factor (HIF)-1 $\alpha$  under hypoxic conditions.<sup>21</sup> While numerous studies have combined scaffold systems with the controlled release of angiogenic factors (e.g., insulin growth factor-I, hepatocyte growth factor,<sup>22</sup> and basic fibroblast growth factor<sup>23</sup>), pleiotropic signaling mediators such as NO<sub>2</sub>-FA have not been applied in this manner. Furthermore, the evaluation of angiogenic factor-controlled release in the application of a temporary scaffold to facilitate abdominal wall tissue reconstruction,<sup>24</sup> and more broadly the evaluation of angiogenesis itself, has been addressed by only qualitative or semiquantitative methods.

In this study, an abdominal wall repair scaffold has been designed based on a microfibrillar PECUU matrix integrated with a hydrogel derived from decellularized porcine dermis and poly(lactic-co-glycolic acid) (PLGA) microspheres loaded with NO<sub>2</sub>-OA. This scaffold was utilized to repair a rat abdominal wall partial thickness defect,<sup>25,26</sup> hypothesizing that the NO<sub>2</sub>-OA release would facilitate increased angiogenesis by 8 weeks. The increased neovascularization, enhanced repair of abdominal wall defects, decreased foreign

body response, and increased cellular ingrowth all supported the conclusion that controlled NO<sub>2</sub>-OA release improved regional angiogenesis. This was characterized by a novel method to quantify vascularization in terms of vessel type and spatial distribution.

## Materials and Methods

### *Polymer synthesis, dermal ECM extraction, and gel preparation*

PECUU was synthesized starting from polycaprolactone diol (PCL,  $M_n$  = 2000; Sigma), polyhexamethylene carbonate diol (PHC,  $M_n$  = 2000; Sigma), and butyl diisocyanate (BDI; Sigma); putrescine was adopted as a chain extender following the protocol described in Hong *et al.*<sup>10</sup> The (PCL + PHC):BDI:putrescine and PCL/PHC molar ratios were 1:2:1 and 1:1, respectively. Thermal properties were measured by differential scanning calorimetry (DSC-60; Shimadzu).<sup>5</sup> Samples were heated to 200°C to erase thermal history, then cooled to -150°C, and heated again to 200°C. All heating and cooling rates were 10°C/min. The polymer utilized had a  $T_g$  of -55°C and a  $T_m$  of 13°C. Based on uniaxial tensile testing, Young's modulus was  $9 \pm 1$  MPa, tensile strength  $21 \pm 2$  MPa, and the strain to failure was  $821 \pm 73\%$ .

Porcine dermal ECM was prepared as reported previously.<sup>27</sup> In brief, full-thickness skin from the dorsolateral flank of market-weight (~260 pounds) pigs was harvested. Subcutaneous fat, connective tissue, and epidermis were mechanically removed. The obtained dermis was subjected to sequential immersion in a vortex shaker at 600 rpm in solutions including 0.25% trypsin, 70% ethanol, 1% TritonX-100 in 0.26% ethylenediaminetetraacetic acid-tetrasodium salt/0.69% Tris, and 0.1% peracetic acid/4% ethanol.

The resulting decellularized tissue samples were then lyophilized and milled into a powder with a commercial Waring<sup>TM</sup> blender and a Wiley Mill. The powder was further processed with 1 mg/mL pepsin (P7012; Sigma) in 0.01 N HCL. Finally, each 0.75 mL of ECM digest was neutralized with 10 $\times$  phosphate-buffered saline (PBS), 0.1 N NaOH (0.075 mL), and 1 $\times$  PBS (0.092 mL) and produced 1 mL of 15 mg/mL ECM solution.

### *Microparticle fabrication*

PLGA microparticles were fabricated by a double emulsion technique originally introduced in Lu *et al.*<sup>28</sup> For the oil component, 0.2 g of PLGA (50:50 wt ratio, 30–60k  $M_w$ ; Sigma) was dissolved in 4 mL of dichloromethane (5% w/v; Sigma), whereas 300  $\mu$ L of 1% PBS/distilled water solution and 60 mL of 2% PBS/polyvinyl alcohol solution were utilized as water one and water two components, respectively. Similarly, the drug was encapsulated in the microparticles<sup>29</sup> by mixing 8.57  $\mu$ L of 10-nitro-9-trans-octadecenoic acid (NO<sub>2</sub>-OA) with 35 mM to the water one component targeting a final molarity of 1 M. The oil–water one emulsion was then created by vortexing for 1 min.

Different particle sizes (Fig. 1A–C, and E) were obtained by setting the agitator at rotation speeds of 1000 and 1500 rpm or by immersing the oil-water beaker in the sonicator bath (Quantrex 90; L&R, Keamy, NJ). Solvent evaporation for 6 h was followed by three sequential distilled water washes with centrifugation (15,000 g for 5 min).

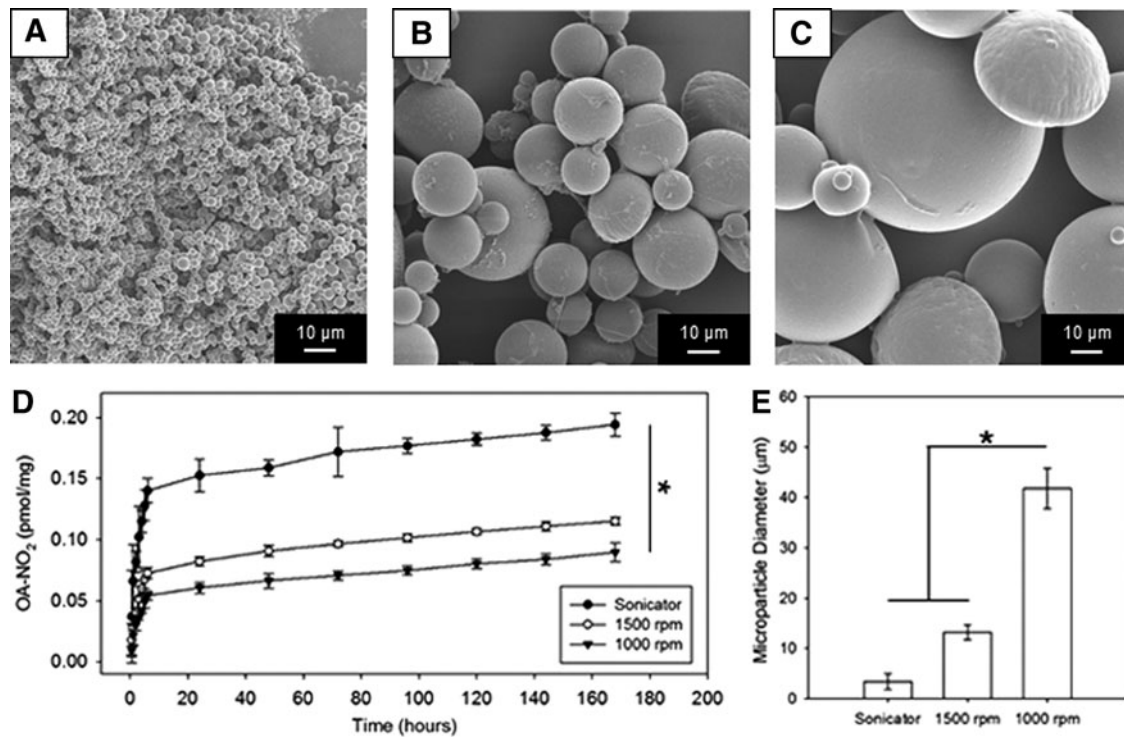


**FIG. 1.** Controlled-release *in vitro* characterization. PLGA microparticle size obtained at different processing conditions: (A) via sonication, (B) or 1500 rpm and (C) 100 rpm agitator speed. (D) NO<sub>2</sub>-OA *in vitro* controlled-release profiles, effects of microparticle size on release kinetics ( $n=3$ ;  $*p<0.05$  at 168 h). (E) Microparticle size quantification,  $*p<0.05$ . NO<sub>2</sub>-OA, nitro-oleic acid; PLGA, poly(lactic-co-glycolic acid).

Freeze-drying for 24 h completed the process, after which the microparticles were collected and stored at  $-20^{\circ}\text{C}$  before integration in the abdominal wall patch.

#### Abdominal wall patch fabrication

Abdominal wall patches were processed by the two stream electrospinning protocol illustrated in D'Amore *et al.*,<sup>11</sup> which was modified to incorporate the microparti-

cles into the scaffold volume. Three types of patches were fabricated (Fig. 2): PECUU electrospun single-layer scaffold with PLGA microparticles not loaded with NO<sub>2</sub>-FA (S), PECUU-ECM bilayered scaffold (S+ECM), and PECUU-ECM bilayered scaffold with integrated PLGA microparticles loaded with NO<sub>2</sub>-OA (S+ECM+D). Hexafluoroisopropanol (HFIP, 12% w/v) was utilized to dissolve the PECUU. A 114 mm diameter cylinder was adopted as an electrospinning target charged at  $-4$  kV, rotating at 750 rpm, and translating

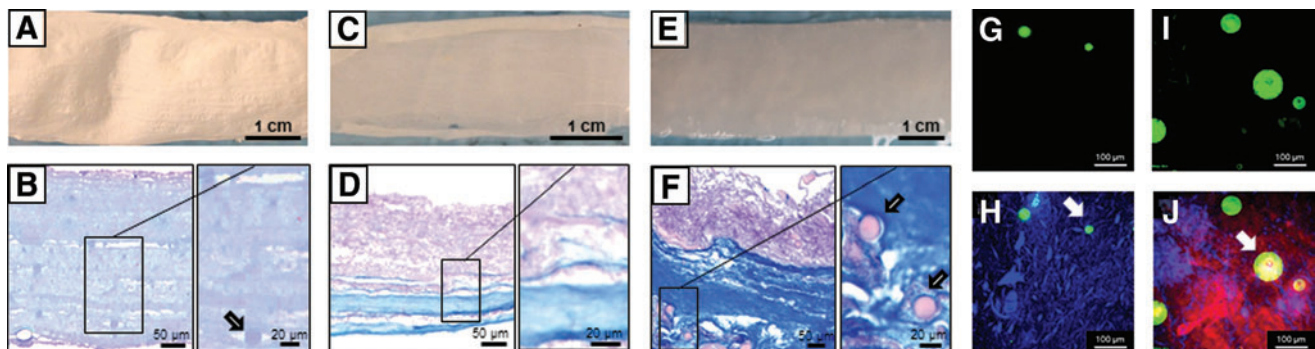


**FIG. 2.** Preimplantation scaffold structure. Visual and histological scaffold structure comparison for the single-layer S group (A, B), for the double-layer S + ECM group (C, D), and for the PLGA microparticle-integrated S + ECM + D group (E, F). Higher magnification *inset* confirmed microparticle or ECM incorporation. Multiphoton image stacks ( $500 \times 500 \times 100 \mu\text{m}$ ): (G) integrated PLGA microparticles and (H) a composite image stack showing a combination of PECUU electrospun fibers and PLGA microparticles for the S group. (I) NO<sub>2</sub>-OA-loaded integrated PLGA microparticles and (J) composite image stack showing PECUU electrospun fibers, dermal ECM gel, and NO<sub>2</sub>-OA-loaded PLGA microparticles for the S+ECM+D group. Arrows in figure (B, F, H, and J) indicate the PLGA microparticles. ECM, extracellular matrix; PECUU, poly(ester carbonate)urethane urea. Color images available online at [www.liebertpub.com/tea](http://www.liebertpub.com/tea)

longitudinally at 0.15 cm/s. The deposition area (4.5 cm in width) was confined by electrical insulating tape and reduced rastering span (6 cm).

The single-layer scaffold was fabricated through wet electrospinning using the following electrospinning processing variables, for stream one (polymer): voltage 13 kV, gap distance 10 cm, and flow rate 20 mL/h. For stream two (PBS), electrospay conditions were as follows: 8 kV, 4 cm gap, and flow rate of 1.35 mL/min. The PBS stream (54 mL) was supplemented with empty PLGA microparticles ( $170 \pm 40$  mg). Total deposition time for all the groups was 40 min.

For the bilayer scaffolds in groups S+ECM and S+ECM+D, the first layer (polymer rich) was fabricated using the same processing conditions described above with a deposition time of 20 min. The remaining 20 min were utilized to form the scaffold second layer (ECM rich), total fabrication time was 40 min. For the S+ECM, the second stream electro-sprayed 15 mg/mL ECM solution with an increased flow rate of 1.5 mL/min while, gaps, voltages, and mandrel kinematics remained unmodified.

Processing conditions for the S+ECM+D group were identical to the S+ECM group with the only exception of the ECM solution (30 mL), which was supplemented with the NO<sub>2</sub>-OA-loaded PLGA microparticles ( $173 \pm 23$  mg). Based on a slower release kinetic described in sections "Controlled release *in vitro* characterization" and "Preimplantation scaffold structure, release profile, and mechanics," the larger diameter microparticles, fabricated at 1000 rpm as described above, were utilized for the animal model.

Finally, S-ECM and S-ECM-D patches were incubated at 37°C for 45 min to induce ECM solution transition to a gelled state. Next, 6 mm diameter circular patches were obtained by a surgical punch. The stiffer scaffold direction was identified by cutting with a surgical blade one edge of the patch parallel to the mandrel tangential speed direction. Metallic parts and tools utilized in the scaffold fabrication and preparation were sterilized. Each side of the generated abdominal patches was sterilized with UV light for 30 min before implantation, which was performed within 12 h of fabrication.

#### Controlled-release *in vitro* characterization

To quantify the impact of fabrication conditions, and more specifically agitator speed and sonication on PLGA microparticle morphology, scanning electron microscopy (SEM) was utilized. Microparticles were sputter-coated with Pd/Au and imaged (grayscale, 8-bit) with SEM (JEOL JSM6330F); NIH Image J was then adopted to quantify microparticle diameter (Fig. 1E).

#### Extraction of NO<sub>2</sub>-OA and controlled release *in vitro*

NO<sub>2</sub>-OA in microparticles and scaffolds was extracted by dissolving the samples in 200  $\mu$ L HFIP with 0.5 pmol NO<sub>2</sub>-[<sup>13</sup>C<sub>18</sub>]OA internal standard, and extracted thrice with 1 mL methanol, each time vortexing and centrifuging at 15,000 *g* for 10 min at 4°C. Then, the collected methanol was dried under a stream of nitrogen, reconstituted in 100  $\mu$ L methanol, and analyzed by high-performance liquid chromatography–electrospray ionization–tandem mass spectrometry (HPLC-ESI-MS/MS).

Controlled release ( $n=3$ ) of NO<sub>2</sub>-OA in microparticles (Fig. 1D) and scaffolds (Fig. 3B) was studied in 50 mM

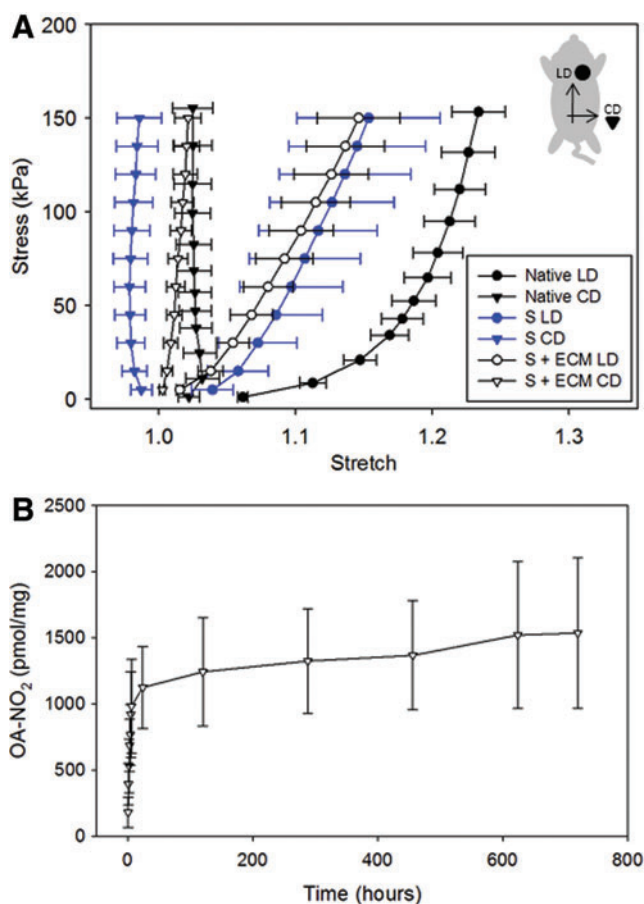


**FIG. 3.** Preimplantation scaffold mechanics and release profile. (A) Scaffold biaxial mechanics characterization (LD and CD indicated the rat longitudinal and circumferential directions, respectively) showed, for a given mandrel velocity, no differences were introduced by microparticle incorporation (S) when compared to the ECM-integrated group (S + ECM). Comparison with native rat abdominal wall planar mechanics from Hashizume *et al.*<sup>8</sup> showed the capacity to duplicate physiologically relevant values of anisotropy ( $n=5$ ). (B) Controlled-release profile for the S + ECM+D group in lipase solution at 37°C up to 1 month ( $n=3$ ). Color images available online at [www.liebertpub.com/tea](http://www.liebertpub.com/tea)

phosphate buffer, pH 7.4 with 0.2 mg/mL porcine lipase at 37°C, as previously.<sup>22</sup> Aliquots were collected at various time points, spiked with 15 pmol NO<sub>2</sub>-[<sup>13</sup>C<sub>18</sub>]OA, 1 mL acetonitrile was added, and then, samples were vortexed, centrifuged, and analyzed by HPLC-ESI-MS/MS. At each time point, a fresh incubating solution was utilized.

#### Liquid chromatography–mass spectrometry analysis of NO<sub>2</sub>-OA

Analysis of NO<sub>2</sub>-OA was performed by HPLC-ESI-MS/MS. The chromatographic system consisted of an analytical C18 Luna column (2 × 20 mm, 5  $\mu$ m; Phenomenex) with a flow rate of 0.75 mL/min and a gradient solvent system of water 0.1% acetic acid (solvent A) and acetonitrile 0.1% acetic acid (solvent B). The gradient program was the following: 35–100% solvent B (0–3 min) and 100% solvent

B (3–4 min) followed by 1 min reequilibration to initial conditions.

The mass spectrometry system consisted of an API4000 Q-trap triple quadrupole mass spectrometer (Applied Biosystems, San Jose, CA) equipped with an ESI source. NO<sub>2</sub>-OA was analyzed in negative mode with the following parameters: declustering potential—75 V, collision energy—35 eV, desolvation temperature of 700°C, and a multiple reaction monitoring (MRM) transition 326.3/46. Quantification of NO<sub>2</sub>-OA in samples was performed by stable isotopic dilution analysis using an NO<sub>2</sub>-OA calibration curve in the presence of NO<sub>2</sub>-[<sup>13</sup>C<sub>18</sub>]OA internal standard (MRM 344.3/46).

#### Multiphoton imaging

Successful integration of PECUU fibers with ECM and microparticles was verified by multiphoton imaging (Fig. 2G–J). Samples ( $n=5$ , each 10×10 mm) were scanned over a 500×500×100 μm volume with multiphoton microscopy at 740 nm excitation wavelength, 5% laser power, and 12.5 μs/pixel sampling speed. Emission channels utilized for the acquisition were 400±50 nm for second harmonic generation originated by the ECM signal, 525±50 nm for the scaffold fibers, and 595±25 nm for the PLGA microparticles.

To facilitate acquisition in these last two channels, polymer fibers and microparticle signals were enhanced with molecular probes.<sup>30</sup> PECUU was supplemented with fluorescein isothiocyanate when dissolved in HFIP, similarly Red CMTX (Molecular Probes) previously mixed with 1 mL of dimethyl sulfoxide was added to the PLGA—solvent solution during the creation of emulsion one in the microparticle processing.

#### Mechanical testing and thermal properties

Preimplant patch mechanics were characterized with biaxial testing ( $n\geq 5$ /group) to verify the efficacy of the scaffold fabrication method to induce anisotropy and stiffness comparable to native tissue<sup>8</sup> (Fig. 3A). Square samples 10×10 mm in size were tested under stress control following a methodology described by Sacks<sup>31</sup>; 150 kPa was estimated as the stress value corresponding to a range of stretch values (1.0–1.20)<sup>8</sup> induced by breathing on the rat abdomen under physiological conditions. Sample thickness was measured with a dial micrometer (L.S. Starrett Co., Athol, MA). Fiducial markers were affixed at the four corners of a 5×5 mm center area within the samples; a deformation gradient tensor was then calculated based on the position of the markers and displacement field derived from shape functions.

Tests were initiated with preconditioning followed by 10 cycles of testing (30 s each) at room temperature in PBS. A free-floating configuration was utilized for the reference system in postprocessing. The ultimate tensile properties of scaffolds in the wet state were evaluated by uniaxial tensile testing employing an MTS Insight (MTS, Eden Prairie, MN) with a 10 N (0.01 N resolution) load cell at room temperature.<sup>10</sup> The samples were extensionally deformed at 10 mm/min according to ASTM D638M. Young's modulus was calculated based on the initial slope of the stress versus strain curve ( $0 \leq \epsilon \leq 10\%$ ) using linear regression. The ultimate stress was determined as the maximum stress.

#### Histology

At 8 weeks postimplantation, samples were retrieved, fixed in 10% formalin solution for  $\geq 24$  h, embedded in paraffin, and serially sectioned into specimens 10 μm in thickness. Next, hematoxylin and eosin (H&E) and Masson's trichrome (MT) staining of preimplantation scaffolds and explants were utilized to evaluate the following: polymeric fiber volume, newly formed tissue, cellular infiltration, and scar area (Figs. 4 and 5). To assess the foreign body response, a custom-made algorithm, developed in Matlab (Mathwork, Natick, MA), was utilized to segment<sup>11</sup> and quantify collagen-rich areas (Fig. 4G, H).

The algorithm is based on a two-phase iterative process known as  $k$  means clustering. In step one, given an integer  $k$  and an array of data,  $k$  cluster centroids were identified minimizing the total squared Euclidean distance between each pixel and its closest RGB centroid.<sup>32</sup> With  $k=4$ , the algorithm segmented each image into four color groups corresponding to background, muscle tissue, collagen or *de-novo* ECM, and scaffold. In step two, collagen pixels were identified as those pixels that had a blue/red pixel intensity ratio of  $\sim 2$ : red <125, blue >210.

At the macroscopic scale, cross-sections were utilized to quantify explant thickness. NIH Image J was utilized to identify the explant central line, draw equispaced segments ( $n=10$ ) perpendicular to this line intersecting the abdominal wall border, and calculate the mean of their lengths. This measure was coupled with *in situ* explant visual inspection (Fig. 6).

#### Animal and surgical models

The animal study was performed following United States National Institutes of Health guidelines for animal care, and was approved by the Institutional Animal Care and Use Committee of the University of Pittsburgh. The experiment was performed in compliance with both the Animal Welfare Act Regulations and Federal statutes relating to animals and experiments involving animals and adhered to the principles defined in the Guide for Care and Use of Laboratory Animals, National Research Council, 1996.

Adult female Sprague-Dawley rats 10–12 weeks old,  $\sim 250$  g in weight (Harlan Sprague Dawley, Inc., Indianapolis, IN), were used for the abdominal wall repair procedure. The experiment was designed to assess the effects of NO<sub>2</sub>-FA controlled release on angiogenesis. Therefore, a partial wall defect was preferred to a full wall defect model; this enabled evaluation of the impact of drug release on the tissue underneath the abdominal wall patch. The surgical protocol was adapted from a procedure previously established.<sup>33</sup>

In brief, inhalation of 1.25–2.5% (maintenance–induction) isoflurane with 100% oxygen was adopted as anesthetic. The skin was shaved and the surgical field was prepared by sterilization with povidone-iodine solution, the rats were positioned in dorsal recumbency on a heating blanket, and the operating environment was kept sterile during the procedure. An incision was made 2 cm inferior to the xiphoid process. Next, a square-shaped partial-thickness defect with a side of 1 cm and a depth of  $\sim 300$  μm was dissected and removed; this included the abdominal wall fascia and part of the muscle; the peritoneum was left intact, while skin and subcutaneous tissue were recomposed at the end of the procedure.

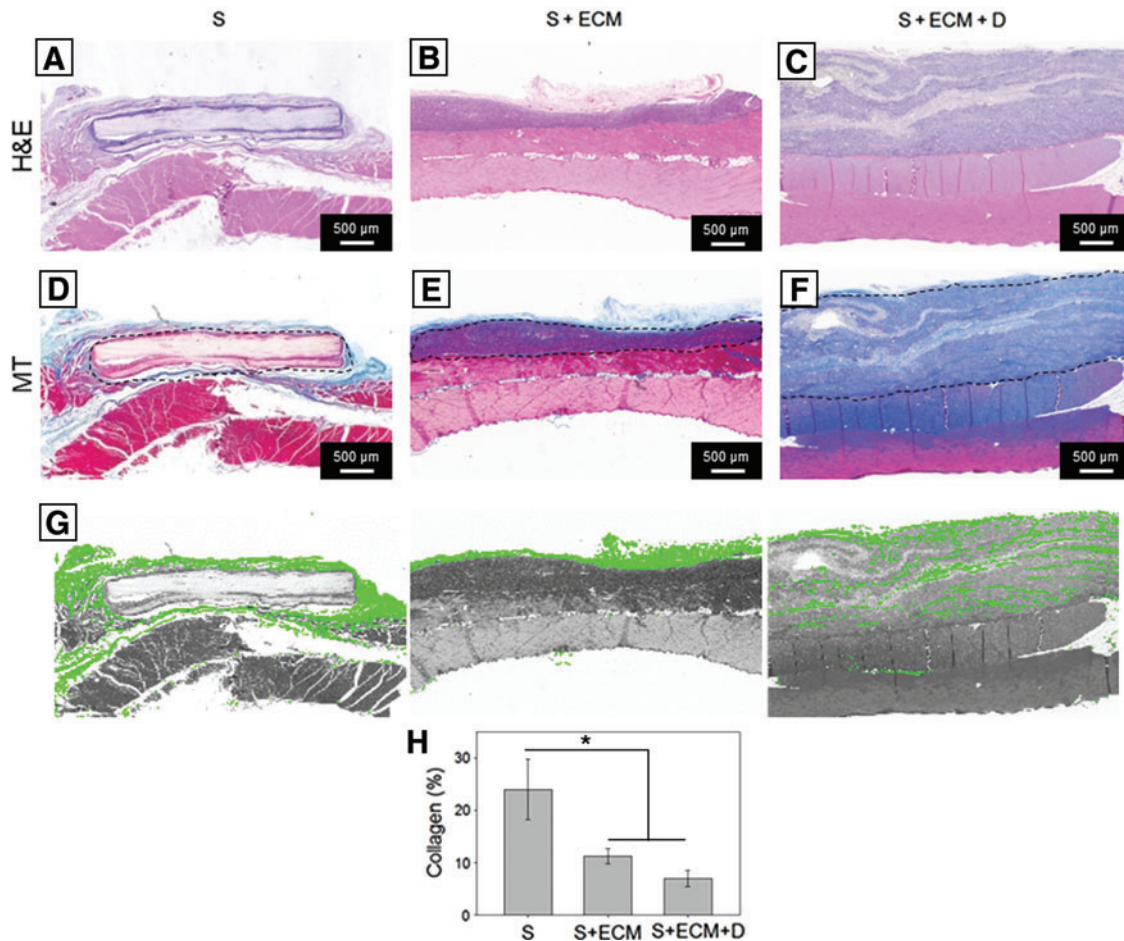


**FIG. 4.** Histological assessment, full cross-sections. H&E and MT staining of 8-week explants for the groups: (A, D) S; (B, E) S + ECM, and (C, F) S + ECM + D. Both qualitative (A–F) and quantitative observation (H) showed reduced fibrous encapsulation and higher cellular infiltration for the S + ECM and S + ECM + D groups when compared to the S group. (G) Examples of collagen/scar area segmentation performed by the developed algorithm. Dotted line indicates the visible part of the scaffold perimeter,  $n \geq 3$ /group,  $*p < 0.05$ . H&E, hematoxylin and eosin; MT, Masson' trichrome. Color images available online at [www.liebertpub.com/tea](http://www.liebertpub.com/tea)

All the patches were sutured by three equal-spaced 7-0 polypropylene sutures to minimize the foreign body response elicited by the polypropylene and better assess the impact of the different scaffolds on angiogenesis. Abdominal wall patches were oriented so that the stiffer direction of the material was aligned with the circumferential direction of the rat abdomen; scaffold notches placed for this purpose (straight edge on disc shaped scaffolds) ensured proper alignment.

S–ECM and S–ECM–D groups were implanted with the ECM component of the scaffold facing the wall defect; this “open face sandwich” approach was meant to promote direct interaction of the ECM component with the treated area. Finally, the skin closure was obtained by double-layer buried suture and the animals remained in the surgical suite under observation until they recovered from anesthesia. Post-operative care followed the standard protocol. Animals were euthanized by isoflurane (5%) inhalation at 8 weeks after the procedure (S group,  $n=6$ , and S+ECM and S+ECM+D,  $n=10$  each). The patches were explanted by cutting ~5 mm outside of the suture line and retrieved samples were processed for histological and immunofluorescence assessment.

#### Blood vessel morphological assessment

Regional angiogenesis was investigated by combining morphological with topological information. Morphological assessment included quantification of blood vessel/mm<sup>2</sup> and vessel type and was performed with two distinct experiments: histological (Fig. 7) and immunofluorescence assessment (Fig. 8).

For the histology, MT-stained cross-sections ( $n \geq 5$  animals/group) were preprocessed as discussed in the Multiphoton imaging section. Explant cross-sections examined with immunofluorescence ( $n \geq 5$  animals/group) were preprocessed with fixation on 4% phosphate-buffered paraformaldehyde solution (4 h), followed by immersion in 30% sucrose solution (>48 h), embedding into OCT compound (Tissue-Tek, Torrance, CA), and finally sectioned with a 10  $\mu$ m step size.

Next, sections were blocked with 10% goat serum in 0.2% Triton 1 $\times$  PBS solution (2 h at room temperature) and treated as in D'Amore *et al.*<sup>11</sup> with mouse primary antibody against CD31 (ab64543, 1:100; Abcam) and rabbit primary antibody against  $\alpha$ SMA (Ab5694, 1:100; Abcam). Anti-rabbit Alexa Fluor<sup>®</sup> 594 (A21207, 1/1000; Thermo Fisher

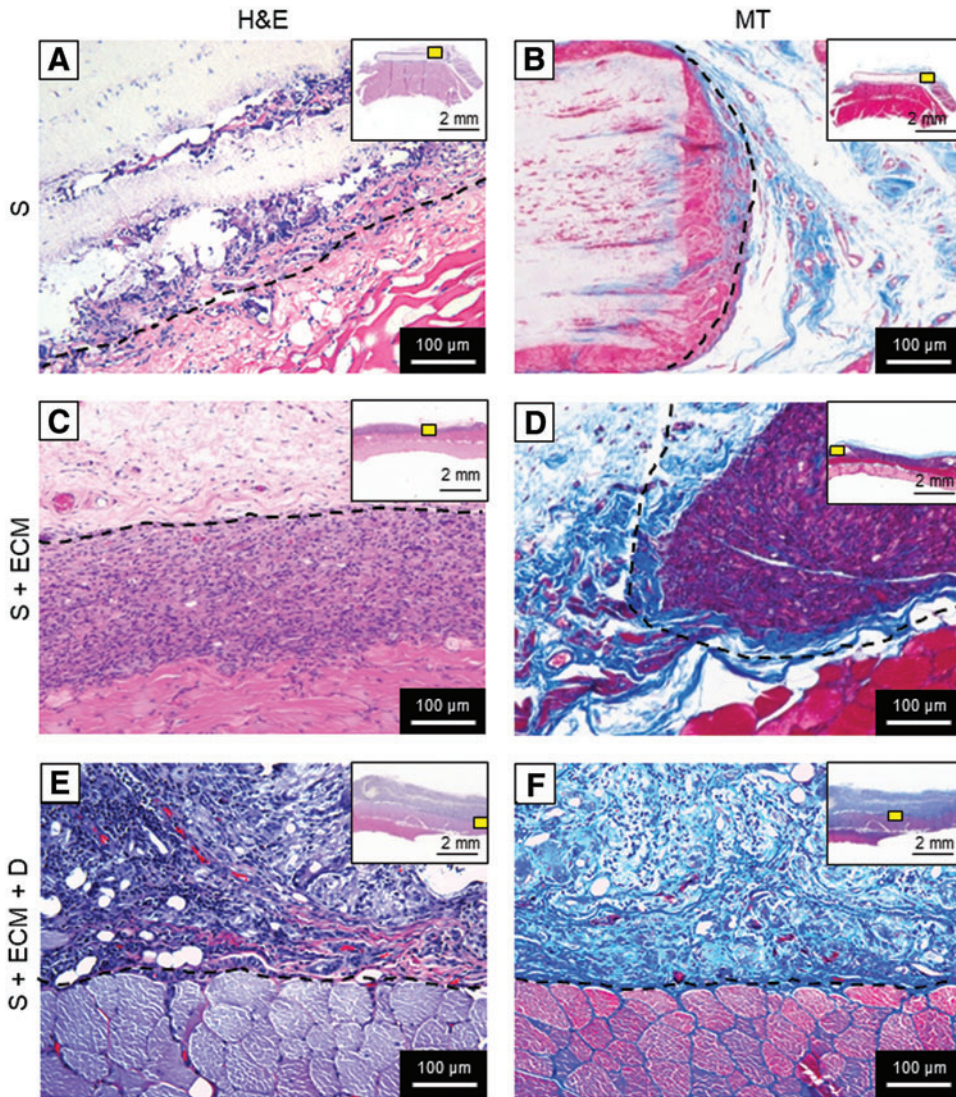


**FIG. 5.** Histological assessment, high magnification. H&E and MT staining of 8-week explants for the groups: (A, B) S, (C, D) S + ECM, and (E, F) S + ECM + D. Qualitative assessment of high magnification (200×) cross-sections at the explant–scaffold interface confirmed higher cellular infiltration for the S+ECM and S+ECM+D groups when compared to the S group. *Top right box* indicates the high magnification field of view position (*yellow box*) with respect to the whole explants. *Dotted line* indicates the visible part of the scaffold perimeter. Color images available online at [www.liebertpub.com/tea](http://www.liebertpub.com/tea)

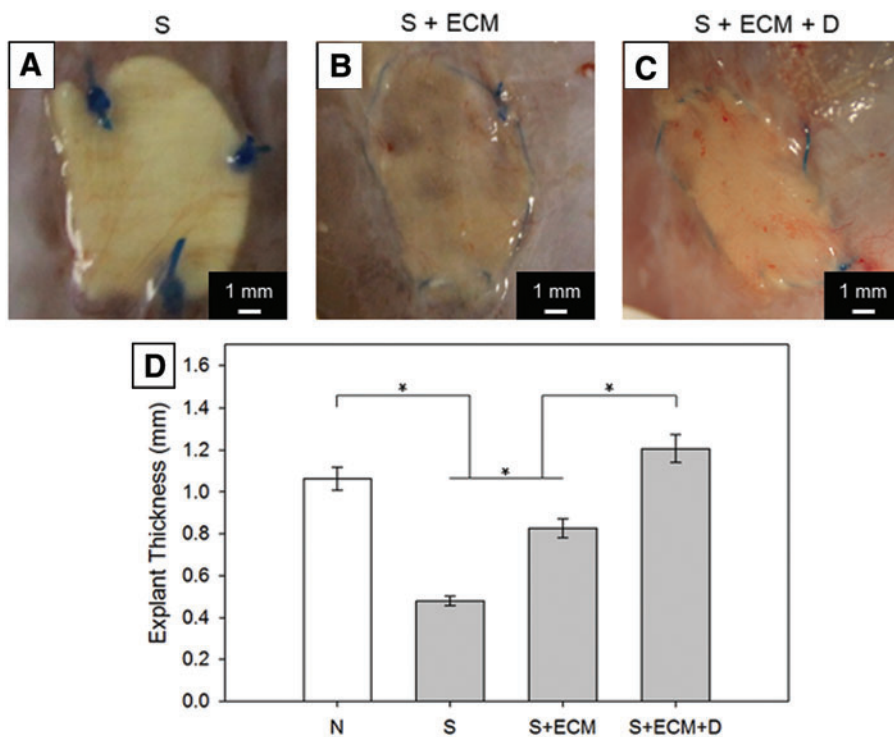


**FIG. 6.** Explant thickness. Visual inspection for the groups: (A) S, (B) S + ECM, and (C) S+ECM+D. (D) Full wall thickness comparison with group N representing the healthy rat abdominal wall thickness, \* $p < 0.05$ . Color images available online at [www.liebertpub.com/tea](http://www.liebertpub.com/tea)

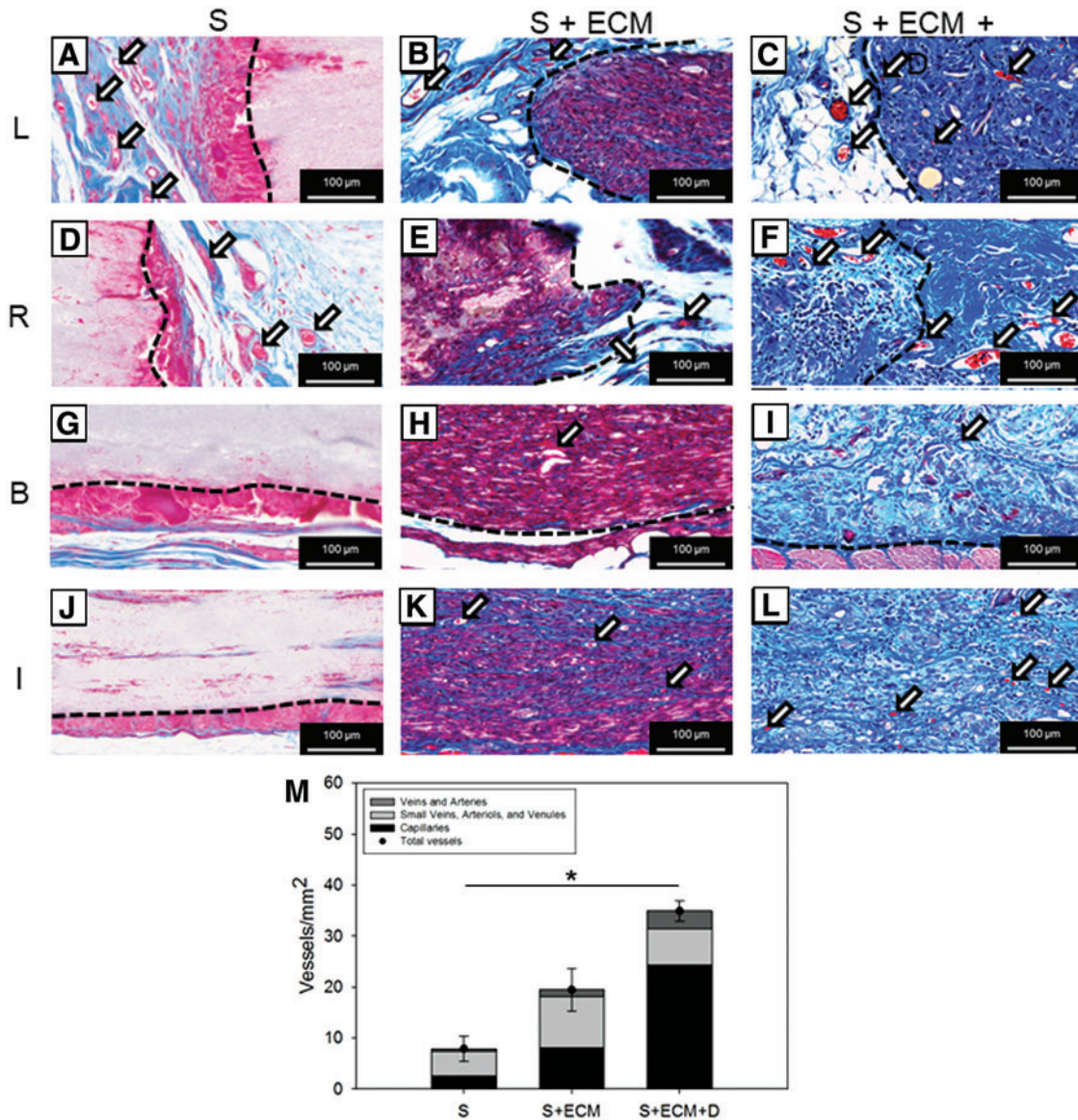


**FIG. 7.** Blood vessel morphological assessment by MT staining. Representative MT staining of 8-week cross-sections at left (L) and right edge (R), below (B) and inside (I) the abdominal wall explants for the groups: (A, D, G, J) S, (B, E, H, K) S+ECM, and (C, F, I, L) S+ECM+D. (M) Blood vessel number and type quantification,  $n \geq 5$ ,  $*p < 0.05$  for total vessels. Arrows in (A–F, H, I, K, L) indicate blood vessels. Details on the adopted algorithm for vessel segmentation are provided in Supplementary Fig. S1. Color images available online at [www.liebertpub.com/tea](http://www.liebertpub.com/tea)

Scientific) and biotin-streptavidin Alexa Fluor<sup>®</sup> 488 (BA-2001, 1:200; Thermo Fisher Scientific—532354, 1:150; Invitrogen) were utilized as secondary antibodies. 4',6-diamidino-2-phenylindole mounting medium was utilized to provide nuclear staining (5  $\mu$ L/section, DAPI H-1200; Vectashield), while negative controls were obtained from sections only processed with secondary antibody.<sup>34,35</sup>

A Nikon Eclipse 6600 microscope (Nikon Corporation) equipped with spectral unmixing of autofluorescence system Nuance 3.0.2 (Caliper Life Science, Inc.) was utilized to acquire epifluorescent images and decouple the signal of interest from autofluorescence generated by muscle tissue and scaffold.<sup>36</sup> Each MT and CD31/ $\alpha$ SMA slide was systematically imaged at 200 $\times$  (Fig. 9A) covering an extensive region, including the area occupied by the abdominal wall patch

(inside: I1, I2, I3), the region underneath (below: B1, B2, and B3), and the region in proximity to the edges where the material was sutured to the native tissue (left and right: L, R).

Blood vessel number and type were then identified and categorized in different groups with an algorithm (Supplementary Figs. S1 and S2; Supplementary Data are available online at [www.liebertpub.com/tea](http://www.liebertpub.com/tea)) utilizing five morphological criteria: (1) diameter size (spanning from 3.7  $\mu$ m for capillaries to 76  $\mu$ m for veins<sup>37</sup>), (2) presence of functionally heterogeneous layers (e.g., tunica intima, media, and adventitia), (3) layer thickness ratios (e.g., predominant tunica media/comparable intima and media), (4) shape (e.g., rounded/amorphous), and (5) cell type in proximity of the object of interest.

The method, previously utilized in D'Amore *et al.*,<sup>11</sup> allowed for the segmentation of the identified vessels into four

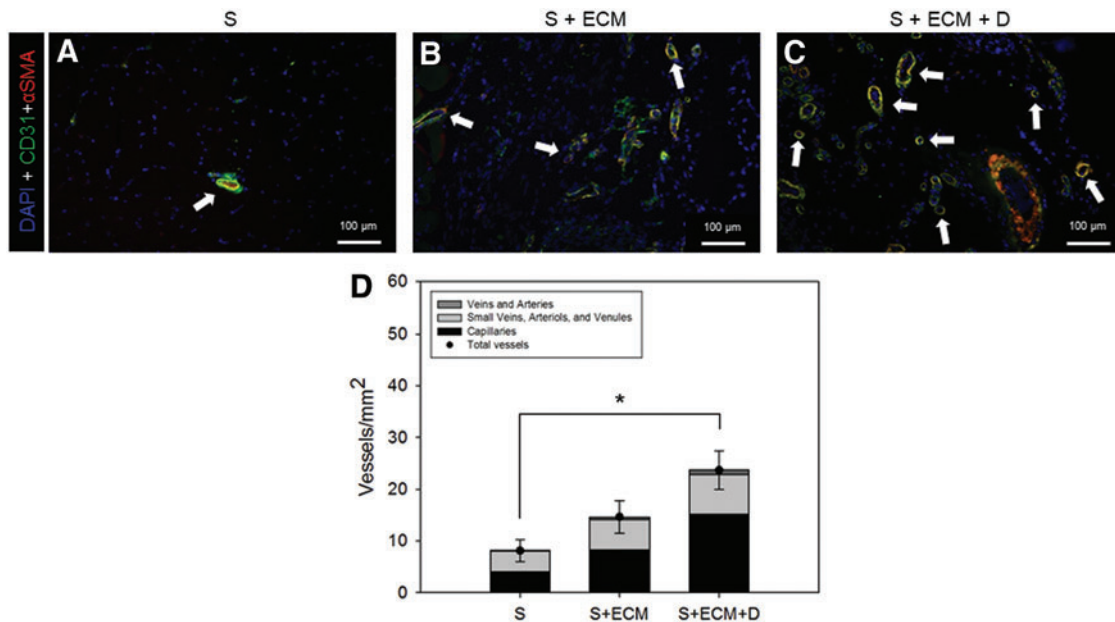


**FIG. 8.** Blood vessel morphological assessment by immunofluorescence staining. Representative DAPI (blue), CD31 (green), and  $\alpha$ SMA (red) co-staining of 8-week cross-sections (region I) for the groups: (A) S, (B) S+ECM, and (C) S+ECM+D. (D) Blood vessel number and type quantification,  $n \geq 5$ ,  $*p < 0.05$  for total blood vessels. Arrows in (A–C) indicate blood vessels. Details on the adopted algorithm for vessel segmentation are provided in Supplementary Fig. S1. DAPI, 4',6-diamidino-2-phenylindole. Color images available online at [www.liebertpub.com/tea](http://www.liebertpub.com/tea)

major categories (i) arterioles and postcapillary veins, (ii) small arteries and venules, (iii) small veins, (iv) arteries and veins. Vessel diameter was measured based on the diameter size of circular cross-sections or based on longitudinal vessel sections. Each detected longitudinal cut of the vessel was considered one count; the diameter was then measured as the distance between the two edges of the vessel.

#### Blood vessel topological assessment

To further investigate the effect of NO<sub>2</sub>-OA release on regional angiogenesis, the images collected and analyzed as described in the previous section were processed with respect to the explant topology. The total number of vessels detected at different locations of each image was averaged and attributed to the geometrical center of the image on a three-dimensional (3D) composite map (combination of eight images Fig. 8A–D) having the volume of the scaffold at its center (white line in Fig. 9B–D) and Z values corresponding to the number of vessels detected. Next, these values were further averaged over the different animals within a given group and interpolated using biquintic numerical interpolation (Matlab; MathWorks).

Values at the upper edge of the explants, representing the animal skin, were set to zero and utilized as a boundary condition for the numerical interpolation (points U1–U5). The 3D surface obtained was then projected over the XY plane where Z values were represented as colors indicating the number of vessels/mm<sup>2</sup>. Finally, additional detail was provided by associating vessel types and their spatial distribution (Fig. 9E–G). This postprocessing strategy allowed for the visualization of color maps describing not only the vessel

number but also their location with respect to the different topological regions. Most importantly, it allowed the identification of different angiogenesis patterns based on the scaffold type.

#### Macrophage infiltration

To assess macrophage infiltration and polarization (Fig. 10), sections were immunolabeled with the pan-macrophage rabbit primary antibody to CD68 (ab125212, 1:100; Abcam), which was coupled with goat anti-rabbit secondary antibody Alexa Fluor 488 (A-1108; 1:1500; Thermo Fisher Scientific). The same sections were also processed with the mouse primary antibody to CD163 (sc-58965, 1:100; Santa Cruz), a macrophage phenotype marker commonly associated with the pro-remodeling (M2-like) phenotype. The secondary anti-mouse antibody was Alexa Fluor<sup>®</sup> 459 labeled (A-11032, 1/200; Invitrogen).

Imaging modality and sample selection were the same utilized for the CD31/ $\alpha$ SMA costaining. CD163 and CD68 positive pixels were identified; their ratio was calculated (Fig. 10E, F) with a custom-made script developed in Matlab based on Otsu's binary segmentation algorithm.<sup>11</sup>

#### Statistical analyses

Statistical analyses were conducted using Sigma plot (Systat Software, Inc., Chicago, IL). One-way analysis of variance (ANOVA) followed by Tukey–Kramer multiple comparison testing was adopted for comparison of multiple samples. To compare the biaxial response of the different groups, one-way ANOVA was applied to compare the maximum stretch at 150 kPa stress level for each sample.

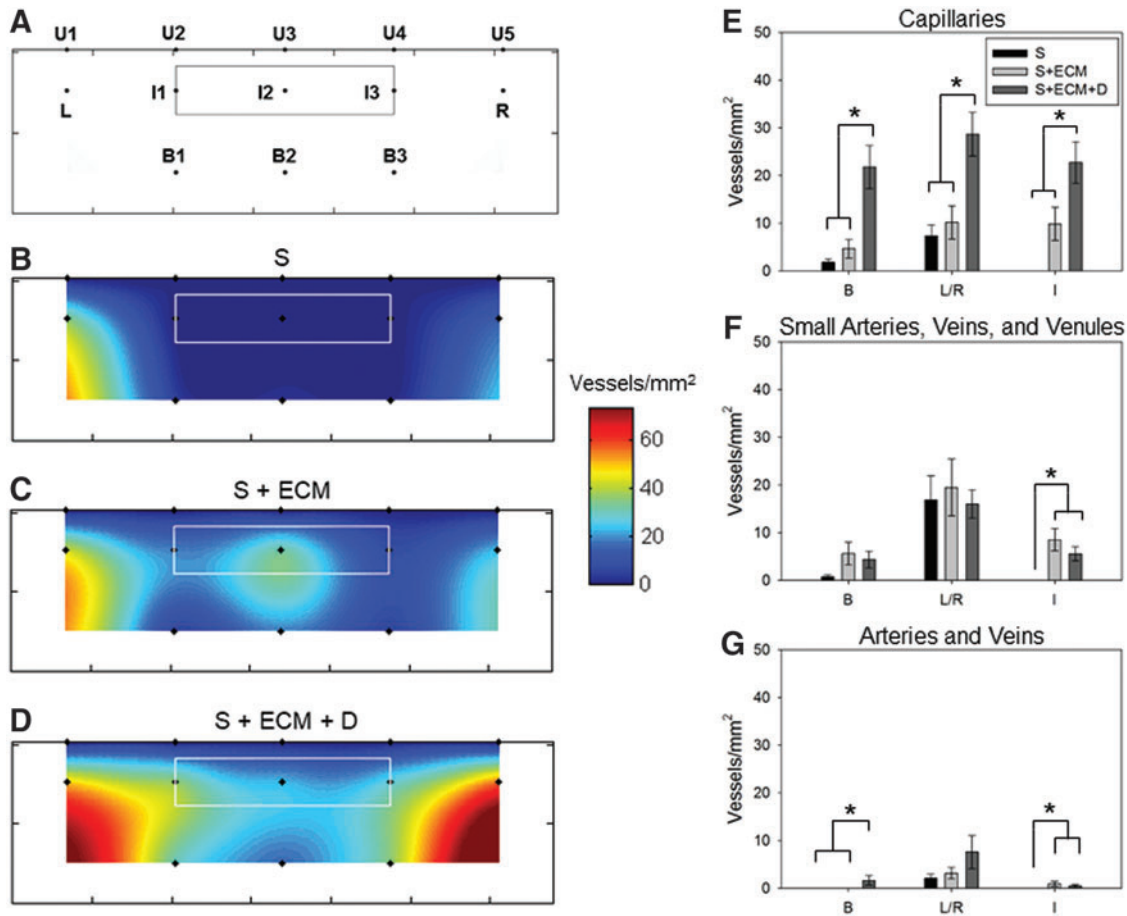


**FIG. 9.** Blood vessel topological assessment. (A) Schematic of the analyzed explants' area. MT cross-sections were imaged at  $200\times$  covering the region occupied by the implanted patch (inside: I1, I2, and I3), the region underneath (below: B1, B2, and B3), and the edges where the material is sutured to the native tissue (left and right: L, R). The solid line around points I1–I3 indicated the approximated border of scaffold, whereas each point corresponded to the geometrical center of each image, and U1–U5 represented the upper border of the explants. Total vessel/mm<sup>2</sup> spatial distribution was provided in (B) for group S, (C) for S+ECM, and (D) for S+ECM+D. Each color map represented the mean of the spatial distribution for blood vessels detected on  $n\geq 5$  animals. Distinct patterns identified for angiogenesis and illustrated in (B–D) were quantified and sorted based on vessel morphology with (E) showing spatial distribution of capillaries (B, L/R, and I indicated the three different regions: below, edges, and inside). Distribution of small arteries, veins, and venules was provided in (F), while (G) offered the quantitative topological assessment for arteries and veins. For (E–G),  $n\geq 5$ ,  $*p < 0.05$  between the scaffold groups. Color images available online at [www.liebertpub.com/tea](http://www.liebertpub.com/tea)

Results are presented as mean  $\pm$  standard error of the mean. Differences were considered to be statistically significant when  $p < 0.05$ .

## Results

### Controlled-release in vitro characterization

The ability to control particle size by changing the agitator speed or by utilizing sonication during the double emulsion processing was qualitatively verified by SEM (Fig. 1A–C); results were corroborated by diameter quantification that showed larger microparticles being produced at 1000 rpm (Fig. 1E). This yielded different surface/volume ratios that, given the same PLGA chemistry and NO<sub>2</sub>-OA quantity for the three groups of particles, produced significantly different release profiles (Fig. 1D).

The microparticles fabricated at 1000 rpm had the smallest surface/volume ratio and as such were characterized by the slowest release profile. One intention of the scaffold design endpoints was to extend the *in vivo* drug release; therefore based on this *in vitro* characterization, the 1000 rpm-induced microparticles were incorporated in the polymeric matrix and utilized for the rest of the study.

### Preimplantation scaffold structure, mechanics, and release profile

Scaffold visual and histological comparisons are provided in Figure 2A–F. MT-stained sections highlighted the single polymer layer structure in the S group, the presence of distinct polymer-rich and ECM-rich layers for the S+ECM and S+ECM+D groups, and the successful integration of microparticles within the ECM-rich component of the S+ECM+D

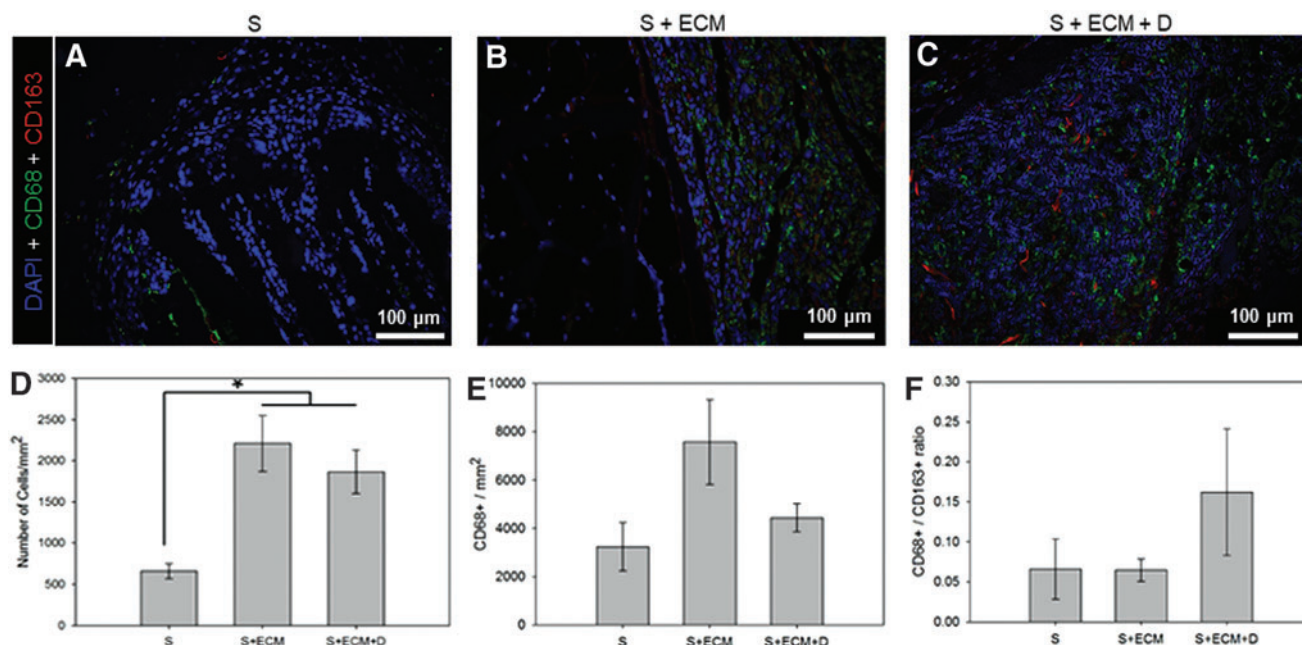


**FIG. 10.** Macrophage infiltration. Representative DAPI (blue), CD68 (green), and CD163 (red) co-staining of 8-week cross-sections (region I) for the groups: (A) S, (B) S+ECM, and (C) S+ECM+D. (D) Cell infiltration by DAPI staining. (E) Macrophage infiltration, quantification performed on CD68+ cells. (F) Macrophage polarization by CD68+/CD163+ ratio. Color images available online at [www.liebertpub.com/tea](http://www.liebertpub.com/tea)

group. The latter was further verified with multiphoton microscopy, with a representative image stack provided in Figure 2G–J and Supplementary Video S1. The microparticle signal acquired by the 595 nm channel (Fig. 2H) enabled the quantification ( $n=5$ ) of the number of particles/volume of scaffold and the corresponding pmol of NO<sub>2</sub>-OA (Table 1).

Given an estimated scaffold preimplantation volume of 39.3 mm<sup>3</sup> and a concentration of particles equal to 260/mm<sup>3</sup> (Table 1), ~10,000 microparticles were included. Scaffold biaxial characterization (Fig. 3A) showed the effects of mandrel velocity, microparticles,<sup>38</sup> and ECM incorporation<sup>11</sup> on patch anisotropy. Moreover, comparison with native abdominal wall mechanics<sup>8</sup> showed the capacity to recapitulate a physiologically relevant level of anisotropy. The controlled-release profile for the S+ECM+D group in lipase solution at 37°C shown in Figure 3B completed the preimplantation sample characterization.

#### Histological assessment

Histological assessment of 8-week explants performed with H&E and MT staining showed reduced fibrous encapsulation and higher cellular infiltration (Figs. 4, 5, and 10D) for the S+ECM and S+ECM+D groups when compared to the S group. Significant thickness differences were detected (Fig. 6), showing beneficial and incremental effects of

ECM incorporation and NO<sub>2</sub>-OA release, respectively. Results of immunolabeling with pan-macrophage marker CD68 and M2-specific marker CD163 are shown in Figure 10.

#### Blood vessel morphological assessment

MT staining of 8-week cross-sections was utilized to quantify blood vessel number/mm<sup>2</sup> and type. Representative images in Figure 7A–F provided examples of vessel formation in proximity to the suture region and underneath the implanted scaffold, respectively. Results of the related quantitative analysis are provided in Figure 7G, showing a significantly higher number of vessels/mm<sup>2</sup> for the S+ECM group when compared to the S group and an even stronger angiogenic effect associated with the loading of NO<sub>2</sub>-OA microparticles.

To further verify this finding, immunofluorescence staining and image analysis were performed. Qualitative observation (Fig. 8A–C) and quantitative measurement (Fig. 8D) showed an increase in vessels/mm<sup>2</sup> for the S+ECM+D group. Both MT and immunofluorescence evaluation offered an additional level of detail by providing vessel-type quantification (Figs. 7G and 9D).

#### Blood vessel topological assessment

Blood vessel topological distribution showed a lack of neo-vessel formation for the S group on regions inside and below the scaffold (Fig. 9B, regions I, B) and weak vessel growth at the edges (Fig. 9B, regions L–R). In contrast, the presence of ECM was associated with blood vessel formation at the core, below, and at the edges of the abdominal wall patch (Fig. 9C). NO<sub>2</sub>-OA release in the S+ECM+D group further emphasized this effect with the highest level of vessels/mm<sup>2</sup> at the edges (Fig. 9D, regions L–R). Data

TABLE 1. SCAFFOLDS' PARTICLE DENSITY

Volume (mm <sup>3</sup> )	0.025
Particles (#)	6.5 ± 1.6
Particles/volume (#/mm <sup>3</sup> )	260 ± 62
NO <sub>2</sub> -OA (pmol/mg)	31.8 ± 1.8

NO<sub>2</sub>-OA, nitro-oleic acid.

were also organized to couple the topological and morphological information, and showed a significantly greater number of capillaries (Fig. 9E) in the S + ECM + D scaffolds regardless of the region.

Small arteries, veins, and venules were more numerous in the I1–I3 regions for the S + ECM and S + ECM + D groups when compared to the S group (Fig. 9F). Finally, the number of larger and more mature vessels/mm<sup>2</sup> such as arteries and veins was significantly greater in the S + ECM + D, B1–B3, and I1–I3 regions (Fig. 9G). Distinct patterns of angiogenesis (Fig. 9) were consistent with the cellular infiltration and fibrotic response illustrated by the histological analysis.

## Discussion

### Controlled-release in vitro characterization

The degradation profile and the release mechanisms of polymeric microparticles/nanoparticles can be modified by a number of factors, including polymer molecular weight (e.g., for PLGA 14k–213k Da),<sup>39</sup> copolymer composition (e.g., for PLGA 85:15, 65:35, and 50:50),<sup>39</sup> morphology (e.g., surface topography and nanochannels),<sup>40</sup> or diameter size.<sup>41</sup> *In vitro* results (Fig. 1) showed the capacity to control the release kinetic of NO<sub>2</sub>-OA (1 mM) up to 7 days by changing the particle size in the 1–50 μm range (Fig. 1D). Consistent with Berkland *et al.*,<sup>41</sup> release profiles were sigmoidal with larger microparticles inducing a slower release.

Controlled release from nonwoven nanofibrous biodegradable scaffolds was previously demonstrated in Kim *et al.*<sup>42</sup> where antibiotic drug was combined with electrospun PLGA fibers for the prevention of postsurgical adhesions and infections. Whether drug is loaded into the polymeric fibers or into carried microparticles, the host interacts directly with the release vehicle impacting directly on its degradation. Lu *et al.*,<sup>28</sup> for example, reported half-lives of 5.5–20.3 days for PLGA microparticles, releasing transforming growth factor β1 in PBS solution.

Aiming to extend the rat abdominal wall exposure to NO<sub>2</sub>-OA, the expected half-lives of PLGA particles were prolonged by the incorporation of the particles into the polymer matrix and/or ECM gel.<sup>29</sup> To simulate *in vitro* a more realistic mechanism, degradation conditions in a static PBS solution<sup>29</sup> were replaced by rocking the samples in a porcine lipase solution at 37°C (Fig. 3B).<sup>22</sup>

### Preimplantation scaffold structure, release profile, and mechanics

While gross appearance and surgical handling of the abdominal wall patches remained consistent across groups (Fig. 2A, C, and E), differences in structure were highlighted with MT staining of cross-sections. S–ECM and S–ECM–D groups showed an open-phase bilayered structure similar to that in D'Amore *et al.*<sup>11</sup> with a clear distinction (Fig. 2B, D, and F) between the polymer-rich and the ECM-rich regions. In contrast, group S had a simpler, single-layer porous structure comparable with the scaffold produced by wet electrospinning in Hashizume *et al.*<sup>8</sup>

Microparticle inclusion and spatial distribution were confirmed by histological analysis of scaffold cross-sections (Fig. 2B, D, and F) and with 3D detail by multiphoton microscopy (Fig. G–J and Supplementary Video S1). The latter

enabled the quantification of the number of particles per unit volume and the pmol NO<sub>2</sub>-OA/mg of scaffold (Table 1). Prospectively, this technique can be crucial to estimate the total amount of drug/scaffold and investigate the therapeutic dose of the compound to be released. The *in vitro* release profile of the implanted S–ECM–D group (PLGA loaded with 1 M NO<sub>2</sub>-OA) remained sigmoidal (Fig. 3B) for up to one month under accelerated degradation conditions.

The effects of mandrel velocity,<sup>38</sup> microparticle integration,<sup>43</sup> and ECM inclusion<sup>11</sup> on biaxial mechanics shown in Figure 3A were in agreement with previous studies, and demonstrated the capacity to recapitulate physiologically relevant values of anisotropy for the rat abdominal wall (e.g., an equistress 150 kPa produces  $\lambda_{PD}=1.0$ – $1.05$ ,  $\lambda_{XD}=1.2$ – $1.25$ <sup>8</sup>). Similarly, for the PECUU polymeric material, the Young's modulus, ultimate stress,  $T_g$ , and  $T_m$  for PECUU were consistent with values reported in Hong *et al.*<sup>10</sup>

### Histologic assessment

There were profound differences between groups in terms of cellular infiltration, scaffold degradation, fibrotic response (Figs. 4 and 5), and abdominal wall thickness (Fig. 6). As for comparative evaluations of electrospun polyurethane and biohybrid (polyurethane + ECM) scaffolds,<sup>44</sup> the S group was less infiltrated by host-recruited cells, the scaffold volume was less degraded, and a stronger encapsulating tissue response was observed (Fig. 4G, H), in contrast to the histological observations with the S + ECM and S + ECM + D groups. Comparison of xenogeneic porcine small intestinal submucosa (SIS) versus polypropylene mesh (PPM) for the repair of abdominal wall defects in a large animal model<sup>45</sup> showed major benefits of biologic material-derived patches when compared to woven synthetic surgical meshes.

In particular, SIS showed better tissue in-growth and fewer adhesions than the PPM. Since then, more than two decades of research has confirmed the better outcomes of SIS materials,<sup>46</sup> for example, assessed tensile strength, collagen formation, and angiogenesis in a rat hernia model repaired with Surgisis® (porcine SIS-derived graft), AlloDerm® (acellular human tissue skin-derived graft), or Vicryl Woven Mesh® (absorbable synthetic, nonantigenic mesh).<sup>47</sup> Consistent with the histological findings of this study when an ECM component was included (Figs. 4 and 5), Surgisis and AlloDerm both showed better collagen deposition, enhanced tissue remodeling, and cellular in-growth.<sup>47</sup>

Despite the positive outcomes associated with biologically derived scaffolds, there are reports of complications with this class of material. Human acellular dermal matrix induced severe inflammation in an adult vervet monkey model.<sup>48</sup> Similarly, Wotton and Akoh<sup>49</sup> reported a clinical case of rejection for Permacol®, a porcine dermis collagen mesh. Lee *et al.*<sup>50</sup> reviewed perioperative and long-term outcomes of porcine dermal matrix for human abdominal wall repair and reported a 42% postsurgery complication rate, which included a 27% incidence of hernia recurrence. These reports have stimulated interest in alternative solutions such as the biohybrid approach presented in this study.

Improved host cell infiltration and reduced material encapsulation, noted histologically (Figs. 4, 5, and 10D), were also corroborated at the macroscopic level by wall thickness

measurements of explants at 8 weeks, where the S+ECM+D group showed the closest value to the healthy native abdominal wall (Fig. 6). The histologic evidence cumulatively suggested beneficial effects of controlled, regional NO<sub>2</sub>-OA release. Wall thickness measurements were also comparable with previous studies (range: 0.8–1.6 mm<sup>8,51</sup>) utilizing elastomeric polyurethane fibrous scaffolds, including those incorporating muscle-derived stem cells, in the same animal model and at the 8-week time point.

#### Blood vessel morphological assessment

Neovascularization is widely recognized<sup>8,46–48,52,53</sup> as a key metric reflecting both positive and adverse outcomes of biomaterials and engineered constructs for abdominal wall repair. Yet, blood vessel morphology, type, and spatial distribution remain generally unaddressed. Most commonly, qualitative evaluation of von Willebrand factor or CD31 immunostaining, MT, and H&E histological sections<sup>48,52,53</sup> is employed to quantify the number of vessels on randomly selected high-magnification images (e.g.,  $n=4$  at  $40\times$ ,  $n=7–10$  at  $100\times$ <sup>8,51</sup>) without performing vessel segmentation based on morphology and spatial distribution.

This study provided increased quantitative insight into angiogenesis by evaluating two independent indices: MT staining and immunofluorescence by CD31 and  $\alpha$ SMA colocalization.<sup>11</sup> According to both methodologies (Figs. 7 and 8), the S+ECM+D group reported greater angiogenesis at 8 weeks compared to the other groups. Although cellular infiltration was greater when ECM was present in the scaffolds, macrophage infiltration (Fig. 10) did not show significant differences between the groups. Comparison between the S and the S+ECM groups in Figure 7 shows a significant effect of the ECM integration on the number of vessels/mm<sup>2</sup>.

An additional effect is then produced by the controlled release of NO<sub>2</sub>-OA as shown by the comparison of the S+ECM+D versus the S and S+ECM groups in Figures 7 and 8. Blood vessels were also segmented within three different categories: (i) capillaries, (ii) small arteries, veins, and venules, and (iii) arteries and veins (Figs. 7 and 8) based on a multicriteria algorithm (Supplementary Fig. S1). The total number of identified vessels/mm<sup>2</sup> was in agreement with previous, less-specific quantification (30–40/mm<sup>2</sup> 8) performed on comparable biomaterials and animal model.

#### Blood vessel topological assessment

The additional detail provided by the assessment described in the previous section was complemented with topological mapping of neovessels (Fig. 9). While section location had a profound effect on outcomes of histologic evaluation, many analyses<sup>8,46–48,52,53</sup> have not addressed this factor, imaging random areas in the region of interest. Averaging over a spatial region of interest might lead to the loss of relevant information. For instance, areas occupied by surgical sutures or at the tissue-biomaterial interface are characterized by a more robust inflammatory response at early time points. The bulk of the scaffold volume is less likely to be infiltrated with cells than the periphery. Drug release will also be spatially dependent and can differentially affect the tissue directly underneath the scaffold more than distal tissue sections.

The present study overcomes these limitations by systematically mapping angiogenesis inside and around the abdominal patch volume. Groups differed in terms of the bulk number of vessels and also revealed distinct vascular growth patterns (Fig. 9B–D). The S group, consistent with the rest of the histological evaluation (Figs. 4 and 5), was mostly engulfed into a collagen capsule and showed only limited vessel growth at the patch edges (Fig. 8B, E, F, and G, regions L and R). In contrast, the ECM component within the S+ECM group was associated with cell infiltration and vessel growth at the core of the scaffold, where small arteries, veins and venules, as well as arteries and veins were more frequently observed compared to the S group (Fig. 9C, E, F, and G region I).

The impact of local differences in NO<sub>2</sub>-OA concentrations in the S+ECM+D group (Fig. 9D) was significant for capillaries in three regions: below (B), inside (I) and at the edges (L and R) (Fig. 9E). Significant differences were also measured for the small arteries, veins and venules (Fig. 9F), with the region inside the scaffold with the S+ECM+D exhibiting more vessels than the S group. This was also the case for the arteries and veins category in regions (Fig. 9G) below and inside the scaffold. As expected, capillaries were the most abundant, regardless of the group, followed by small arteries, veins and venules and finally by larger arteries and veins.

#### Abdominal wall repair and enhanced angiogenesis: technology overview

Alternatives to autologous tissue<sup>2</sup> for abdominal wall repair include a vast spectrum of biomaterials and tissue engineering approaches. Early attempts focused on improving performance and resistance to adhesion of nondegradable woven surgical meshes,<sup>54,55</sup> yet the increasing clinical success of biologic scaffolds gave impetus to a shift toward the development of ECM-based meshes such as decellularized xenogenic dermis<sup>49,50,53,56</sup> or SIS,<sup>45–47</sup> decellularized allogeneic tissue,<sup>48,57,58</sup> decellularized and then cell-seeded xenogeneic tissue<sup>52</sup> and decellularized bovine pericardium.<sup>59</sup> This class of biomaterials has generally achieved favorable endpoints in terms of *in situ* remodeling with cases showing long term evidence of new skeletal muscle fiber formation and innervations.<sup>52</sup>

Despite these achievements, witnessed by the large number of biological surgical meshes now being used clinically,<sup>25,60</sup> postsurgical hernia recurrence remains problematic,<sup>50</sup> and control over the structure and function of abdominal wall support devices is still limited.<sup>6</sup> This motivates the introduction of alternative paradigms capable of balancing the higher level of processing control associated with synthetic materials and the superior bioactivity of ECM-derived meshes. Experience with biodegradable woven meshes,<sup>7</sup> as opposed to devices designed to remain permanently in the host,<sup>54,55</sup> can reduce the risk of chronic inflammation while mitigating mechanical mismatch at the tissue-device interface.

Incorporation of an ECM component, such as including cell seeded synthetic–biologic composite woven constructs<sup>61</sup> or biohybrid and biodegradable nonwoven scaffolds,<sup>8,51,62</sup> may also provide improved biological response and less risk for chronic morbidity. While adverse effects in terms of immune response to the scaffold implantation can be equally induced by a biological as well as by a biohybrid

material, the adoption of ECM scaffolds (not integrated with a polymeric matrix) limits control of patch morphology and mechanics. Key biomaterial features such as: pore size, pore interconnectivity, elastic modulus, and tissue anisotropy, depend on the tissue source and are fundamentally affected by the decellularization process.

A recognized advantage of the bio-hybrid approach is the ability to combine bioactivity associated with the biological material with greater control of the structure–function relationships, as is typical with synthetic material processing methods. Regional angiogenesis is often noted as a critical factor related to positive clinical outcomes. However, virtually no biomaterials and tissue constructs specifically focus on approaches that facilitate and sustain neovascularization.

#### *Activity of NO<sub>2</sub>-OA in abdominal wall repair*

NO<sub>2</sub>-OA, as a thiol-reactive electrophilic fatty acid, will be by nature a pleiotropic signaling mediator. The unique nature of nitro-alkene substituents promotes both kinetically rapid and reversible Michael addition reaction.<sup>12</sup> These data support that the posttranslational protein modification reactions, including those with adaptive signaling mediators such as Keap1/Nrf2, sEH, PPAR $\gamma$ , and NF- $\kappa$ B p65 subunit, are nontoxic and induce anti-inflammatory responses.<sup>16–18</sup> The preclinical actions of NO<sub>2</sub>-OA have been reported in murine models of vascular restenosis,<sup>63</sup> cardiac ischemia-reperfusion injury,<sup>16</sup> atherosclerosis,<sup>64</sup> and diabetes<sup>15</sup> among others. A recent study showed that NO<sub>2</sub>-OA decreases myocardial fibrosis and modulates functional polarization of M1 and M2 macrophage subpopulations.<sup>65,66</sup>

These results are consistent with the present abdominal wall repair and macrophage infiltration responses. While there were no statistically significant differences between proinflammatory (M1 like) and proremodeling (M2 like) macrophage phenotypes, this might be explained by the fact that healthy native abdominal wall conditions were being re-established. Finally, NO<sub>2</sub>-OA activates Nrf2-dependent gene expression,<sup>18</sup> which in turn regulates proangiogenic mediator<sup>67</sup> and HIF-1 $\alpha$  gene expression, stimulating capillary-like sprouts *ex vivo* and angiogenesis in chicken egg membranes.<sup>21</sup> These data reveal that NO<sub>2</sub>-OA promotes neovascularization in the rat abdominal wall by increasing the number of capillaries, small arteries, veins, and venules.

#### *Abdominal wall repair and enhanced angiogenesis: limitations and future work*

A number of limitations can be identified for this study. In the future, shorter (1, 4 weeks) and longer (24 weeks) time points in conjunction with biomechanical functional tests can reveal the impact of vessel formation on muscle regeneration. In addition, a larger animal model and the consideration of the impact of obesity would provide additional perspective for future clinical translation. Moreover, a more mechanistic understanding of how NO<sub>2</sub>-OA affects patterns of tissue gene expression, angiogenesis, inflammation, and tissue remodeling will require further histopathological, biochemical, and dose–response assessments. An additional control group evaluating the effects of PLGA microparticles and ECM incorporation could have been included in the study. Yet, effects of PLGA particles alone on mature vessel formation have not been previously reported.

Few limiting factors affect the vessel morphological assessment; when a longitudinal cut of a vessel was identified, the diameter was measured as the distance between the two edges. This process represents a potential source of error for the vessels/ $\mu\text{m}^2$  measurement since, for a given diameter, a longitudinal cut occupies a much larger area than its corresponding cross-section.

## Conclusions

Postsurgical complications remain associated with devices employed to repair abdominal wall hernias. The biomaterials employed in these devices vary greatly from purely synthetic (e.g., PPMs) to biologic materials based on decellularized xenotypic tissue. While synthetic materials offer controlled structure and mechanics, they lack positive remodeling potential. Biologic materials address the issue of remodeling potential, but sacrifice robust mechanical control. The abdominal wall patch strategy reported in this study demonstrated the benefits of a biohybrid biomaterials approach combined with the controlled release of an angiogenesis facilitating mediator (NO<sub>2</sub>-OA).

Enhanced angiogenesis was demonstrated by a newly described method to spatially quantify vascularization. The three components of the employed composite scaffold design strategy (ECM gel, polymeric fibers, and NO<sub>2</sub>-OA-loaded PLGA microparticles) enable tuning of biomaterial performance characteristics. Scaffold degradation and mechanics can be modified with the polymeric component and processing parameters, while the controlled-release characteristics of the synthetic endogenous mediator homolog can be tuned by changing microparticle/drug loading characteristics. The overall system provides a biomaterial design approach applicable to other tissue augmentation and support settings.

## Acknowledgments

This work was financially supported by RiMED Foundation “Dr D’Amore” research support for years 2013–2016,” the NIH R01-HL058115, R01-HL64937, the Commonwealth of Pennsylvania—Fiscal years 2012–2013, the Pitt EXCEL Program and the Italian Ministry for Education and Research (MIUR). The authors would also like to acknowledge Mr. S. Johnson for assistance in preparing the dermal ECM, Mr. D.E. Jacob and Dr. N. Turner for help with immunofluorescence staining, and Dr. S. Watkins, director of the Center for Biological Imaging, University of Pittsburgh, for providing access to his advanced imaging facility.

## Disclosure Statement

Dr. B.A.F. acknowledges an interest in Complexa, Inc.

## References

1. Rutkow, I.M. Demographic and socioeconomic aspects of hernia repair in the United States in 2003. *Surg Clin North Am* **83**, 1045, 2003.
2. de Vries Reilingh, T., Bodegom, M., Van Goor, H., Hartman, E., van der Wilt, G.J., and Bleichrodt, R. Autologous tissue repair of large abdominal wall defects. *Br J Surg* **94**, 791, 2007.

3. Mudge, M., and Hughes, L.E. Incisional hernia: a 10 year prospective study of incidence and attitudes. *Br J Surg* **72**, 70, 1985.
4. Azzie, G., Maoate, K., Beasley, S., Retief, W., and Bensoussan, A. A simple technique of laparoscopic full-thickness anterior abdominal wall repair of retrosternal (Morgagni) hernias. *J Pediatr Surg* **38**, 768, 2003.
5. den Hartog, D., Dur, A.H.M., Tuinebreijer, W.E., and Kreis, R.W. Open surgical procedures for incisional hernias. *Cochrane Database Syst Rev* (3), CD006438, 2008.
6. Badylak, S.F., Freytes, D.O., and Gilbert, T.W. Extracellular matrix as a biological scaffold material: structure and function. *Acta Biomater* **5**, 1, 2009.
7. Drewa, T., Galazka, P., Prokurat, A., *et al.* Abdominal wall repair using a biodegradable scaffold seeded with cells. *J Pediatr Surg* **40**, 317, 2005.
8. Hashizume, R., Fujimoto, K.L., Hong, Y., *et al.* Morphological and mechanical characteristics of the reconstructed rat abdominal wall following use of a wet electrospun biodegradable polyurethane elastomer scaffold. *Biomaterials* **31**, 3253, 2010.
9. Guan, J., Sacks, M.S., Beckman, E.J., and Wagner, W.R. Synthesis, characterization, and cytocompatibility of elastomeric, biodegradable poly(ester-urethane)ureas based on poly(caprolactone) and putrescine. *J Biomed Mater Res* **61**, 493, 2002.
10. Hong, Y., Guan, J., Fujimoto, K.L., Hashizume, R., Pelinescu, A.L., and Wagner, W.R. Tailoring the degradation kinetics of poly(ester carbonate urethane)urea thermoplastic elastomers for tissue engineering scaffolds. *Biomaterials* **31**, 4249, 2010.
11. D'Amore, A., Yoshizumi, T., Luketich, S.K., *et al.* B-layered polyurethane-extracellular matrix cardiac patch improves ischemic ventricular wall remodeling in a rat model. *Biomaterials* **107**, 1, 2016.
12. Freeman, B.A., Baker, P.R.S., Schopfer, F.J., Woodcock, S.R., Napolitano, A., and d'Ischia, M. Nitro-fatty acid formation and signaling. *J Biol Chem* **283**, 15515, 2008.
13. Fazzari, M., Khoo, N., Woodcock, S.R., Li, L., Freeman, B.A., and Schopfer, F.J. Generation and esterification of electrophilic fatty acid nitroalkenes in triacylglycerides. *Free Radic Biol Med* **87**, 113, 2015.
14. Delmastro-Greenwood, M., Hughan, K.S., Vitturi, D.A., *et al.* Nitrite and nitrate-dependent generation of anti-inflammatory fatty acid nitroalkenes. *Free Radic Biol Med* **89**, 333, 2015.
15. Schopfer, F.J., Cole, M.P., Groeger, A.L., *et al.* Covalent peroxisome proliferator-activated receptor gamma adduction by nitro-fatty acids: selective ligand activity and anti-diabetic signaling actions. *J Biol Chem* **285**, 12321, 2010.
16. Rudolph, V., Rudolph, T.K., Schopfer, F.J., *et al.* Endogenous generation and protective effects of nitro-fatty acids in a murine model of focal cardiac ischaemia and reperfusion. *Cardiovasc Res* **85**, 155, 2010.
17. Charles, R.L., Rudyk, O., Prysyzhna, O., *et al.* Protection from hypertension in mice by the Mediterranean diet is mediated by nitro fatty acid inhibition of soluble epoxide hydrolase. *Proc Natl Acad Sci U S A* **111**, 8167, 2014.
18. Kansanen, E., Bonacci, G., Schopfer, F.J., *et al.* Electrophilic nitro-fatty acids activate NRF2 by a KEAP1 cysteine 151-independent mechanism. *J Biol Chem* **286**, 14019, 2011.
19. Villacorta, L., Chang, L., Salvatore, S.R., *et al.* Electrophilic nitro-fatty acids inhibit vascular inflammation by disrupting LPS-dependent TLR4 signalling in lipid rafts. *Cardiovasc Res* **98**, 116, 2013.
20. Villacorta, L., Gao, Z., Schopfer, F.J., Freeman, B.A., and Chen, Y.E. Nitro-fatty acids in cardiovascular regulation and diseases: characteristics and molecular mechanisms. *Front Biosci (Landmark Ed)* **21**, 873, 2016.
21. Rudnicki, M., Faine, L.A., Dehne, N., *et al.* Hypoxia inducible factor-dependent regulation of angiogenesis by nitro-fatty acids. *Arterioscler Thrombos Vasc Biol* **31**, 1360, 2011.
22. Nelson, D.M., Baraniak, P.R., Ma, Z., *et al.* Controlled release of IGF-1 and HGF from a biodegradable polyurethane scaffold. *Pharmaceut Res* **28**, 1282, 2011.
23. Guan, J., Stankus, J.J., and Wagner, W.R. Biodegradable elastomeric scaffolds with basic fibroblast growth factor release. *J Control Release* **120**, 70, 2007.
24. Wang, L., Lai, D.M., Yang, B., Jiang, Z.P., Zhang, Y.C., Zhou, J., Lai, W., and Chen, S. Reconstruction of abdominal wall defects using small intestinal submucosa coated with gelatin hydrogel incorporating basic fibroblast growth factor. *Acta Cir Bras* **29**, 252, 2014.
25. Brown, B.N., Londono, R., Tottey, S., *et al.* Macrophage phenotype as a predictor of constructive remodeling following the implantation of biologically derived surgical mesh materials. *Acta Biomater* **8**, 978, 2012.
26. Brown, B.N., Valentin, J.E., Stewart-Akers, A.M., McCabe, G.P., and Badylak, S.F. Macrophage phenotype and remodeling outcomes in response to biologic scaffolds with and without a cellular component. *Biomaterials* **30**, 1482, 2009.
27. Reing, J.E., Brown, B.N., Daly, K.A., *et al.* The effects of processing methods upon mechanical and biologic properties of porcine dermal extracellular matrix scaffolds. *Biomaterials* **31**, 8626, 2010.
28. Lu, L., Stamatias, G.N., and Mikos, A.G. Controlled release of transforming growth factor beta1 from biodegradable polymer microparticles. *J Biomed Mater Res* **50**, 440, 2000.
29. DeFail, A.J., Chu, C.R., Izzo, N., and Marra, K.G. Controlled release of bioactive TGF-β1 from microspheres embedded within biodegradable hydrogels. *Biomaterials* **27**, 1579, 2006.
30. D'Amore, A., Amoroso, N., Gottardi, R., *et al.* From single fiber to macro-level mechanics: a structural finite-element model for elastomeric fibrous biomaterials. *J Mech Behav Biomed Mater* **39**, 146, 2014.
31. Sacks, M.S. Biaxial mechanical evaluation of planar biological materials. *J Elastic Phys Sci Solids* **61**, 199, 2000.
32. Arthur, D., and Vassilvitskii, S. k-means++: the advantages of careful seeding. *Proceedings of the Eighteenth Annual ACM-SIAM Symposium on Discrete Algorithms*. Society for Industrial and Applied Mathematics, New Orleans, LA, 2007, pp. 1027.
33. Lai, P.-H., Chang, Y., Liang, H.-C., Chen, S.-C., Wei, H.-J., and Sung, H.-W. Peritoneal regeneration induced by an acellular bovine pericardial patch in the repair of abdominal wall defects. *J Surg Res* **127**, 85, 2005.
34. Fujimoto, K.L., Guan, J., Oshima, H., Sakai, T., and Wagner, W.R. In vivo evaluation of a porous, elastic, biodegradable patch for reconstructive cardiac procedures. *Ann Thorac Surg* **83**, 648, 2007.
35. Hashizume, R., Hong, Y., Takanari, K., Fujimoto, K.L., Tobita, K., and Wagner, W.R. The effect of polymer degradation time on functional outcomes of temporary elastic patch support in ischemic cardiomyopathy. *Biomaterials* **34**, 7353, 2013.

36. Faulk, D.M., Londono, R., Wolf, M.T., *et al.* ECM hydrogel coating mitigates the chronic inflammatory response to polypropylene mesh. *Biomaterials* **35**, 8585, 2014.
37. Wiedeman, M.P. Dimensions of blood vessels from distributing artery to collecting vein. *Circ Res* **12**, 375, 1963.
38. Courtney, T., Sacks, M.S., Stankus, J., Guan, J., and Wagner, W.R. Design and analysis of tissue engineering scaffolds that mimic soft tissue mechanical anisotropy. *Biomaterials* **27**, 3631, 2006.
39. Mittal, G., Sahana, D.K., Bhardwaj, V., and Ravi Kumar, M.N.V. Estradiol loaded PLGA nanoparticles for oral administration: effect of polymer molecular weight and copolymer composition on release behavior in vitro and in vivo. *J Control Release* **119**, 77, 2007.
40. Slowing, I.I., Vivero-Escoto, J.L., Wu, C.-W., and Lin, V.S.Y. Mesoporous silica nanoparticles as controlled release drug delivery and gene transfection carriers. *Adv Drug Deliv Rev* **60**, 1278, 2008.
41. Berklund, C., King, M., Cox, A., Kim, K., and Pack, D.W. Precise control of PLG microsphere size provides enhanced control of drug release rate. *J Control Release* **82**, 137, 2002.
42. Kim, K., Luu, Y.K., Chang, C., *et al.* Incorporation and controlled release of a hydrophilic antibiotic using poly(lactide-co-glycolide)-based electrospun nanofibrous scaffolds. *J Control Release* **98**, 47, 2004.
43. Amoroso, N.J., D'Amore, A., Hong, Y., Wagner, W.R., and Sacks, M.S. Elastomeric electrospun polyurethane scaffolds: the interrelationship between fabrication conditions, fiber topology, and mechanical properties. *Adv Mater* **23**, 106, 2011.
44. Hong, Y., Huber, A., Takanari, K., *et al.* Mechanical properties and in vivo behavior of a biodegradable synthetic polymer microfiber-extracellular matrix hydrogel biohybrid scaffold. *Biomaterials* **32**, 3387, 2011.
45. Clarke, K.M., Lantz, G.C., Salisbury, S.K., Badylak, S.F., Hiles, M.C., and Voytik, S.L. Intestine submucosa and polypropylene mesh for abdominal wall repair in dogs. *J Surg Res* **60**, 107, 1996.
46. Ayubi, F., Armstrong, P., Mattia, M., and Parker, D. Abdominal wall hernia repair: a comparison of Permacol<sup>®</sup> and Surgisis<sup>®</sup> grafts in a rat hernia model. *Hernia* **12**, 373, 2008.
47. Rice, R.D., Ayubi, F.S., Shaub, Z.J., Parker, D.M., Armstrong, P.J., and Tsai, J.W. Comparison of Surgisis<sup>®</sup>, AlloDerm<sup>®</sup>, and Vicryl Woven Mesh<sup>®</sup> grafts for abdominal wall defect repair in an animal model. *Aesthetic Plast Surg* **34**, 290, 2010.
48. Xu, H., Wan, H., Sandor, M., *et al.* Host response to human acellular dermal matrix transplantation in a primate model of abdominal wall repair. *Tissue Eng Part A* **14**, 2009, 2008.
49. Wotton, F.T., and Akoh, J.A. Rejection of Permacol<sup>®</sup> mesh used in abdominal wall repair: a case report. *World J Gastroenterol* **15**, 4331, 2009.
50. Lee, E.I., Chike-Obi, C.J., Gonzalez, P., *et al.* Abdominal wall repair using human acellular dermal matrix: a follow-up study. *Am J Surg* **198**, 650, 2009.
51. Takanari, K., Hashizume, R., Hong, Y., *et al.* Skeletal muscle derived stem cells microintegrated into a biodegradable elastomer for reconstruction of the abdominal wall. *Biomaterials* **113**, 31, 2017.
52. Coppi, P.D., Bellini, S., Conconi, M.T., *et al.* Myoblast-acellular skeletal muscle matrix constructs guarantee a long-term repair of experimental full-thickness abdominal wall defects. *Tissue Eng* **12**, 1929, 2006.
53. Sandor, M., Xu, H., Connor, J., *et al.* Host response to implanted porcine-derived biologic materials in a primate model of abdominal wall repair. *Tissue Eng Part A* **14**, 2021, 2008.
54. Bellón, J.M., Contreras, L.A., Buján, J., and Carrera-San Martín, A. Experimental assay of a Dual Mesh<sup>®</sup> polytetrafluoroethylene prosthesis (non-porous on one side) in the repair of abdominal wall defects. *Biomaterials* **17**, 2367, 1996.
55. Bellón, J.M., Contreras, L.A., Buján, J., Palomares, D., and Carrera-San Martín, A. Tissue response to polypropylene meshes used in the repair of abdominal wall defects. *Biomaterials* **19**, 669, 1998.
56. Mulier, K., Nguyen, A., Delaney, J., and Marquez, S. Comparison of Permacol<sup>™</sup> and Strattice<sup>™</sup> for the repair of abdominal wall defects. *Hernia* **15**, 315, 2011.
57. Bellows, C.F., Albo, D., Berger, D.H., and Awad, S.S. Abdominal wall repair using human acellular dermis. *Am J Surg* **194**, 192, 2007.
58. Eberli, D., Rodriguez, S., Atala, A., and Yoo, J.J. In vivo evaluation of acellular human dermis for abdominal wall repair. *J Biomed Mater Res A* **93**, 1527, 2010.
59. Limpert, J.N., Desai, A.R., Kumpf, A.L., Fallucco, M.A., and Aridge, D.L. Repair of abdominal wall defects with bovine pericardium. *Am J Surg* **198**, e60, 2009.
60. Crapo, P.M., Gilbert, T.W., and Badylak, S.F. An overview of tissue and whole organ decellularization processes. *Biomaterials* **32**, 3233, 2011.
61. Pu, F., Rhodes, N.P., Bayon, Y., *et al.* The use of flow perfusion culture and subcutaneous implantation with fibroblast-seeded PLLA-collagen 3D scaffolds for abdominal wall repair. *Biomaterials* **31**, 4330, 2010.
62. Takanari, K., Hong, Y., Hashizume, R., *et al.* Abdominal wall reconstruction by a regionally distinct biocomposite of extracellular matrix digest and a biodegradable elastomer. *J Tissue Eng Regen Med* **10**, 748, 2016.
63. Cole, M.P., Rudolph, T.K., Khoo, N.K., *et al.* Nitro-fatty acid inhibition of neointima formation after endoluminal vessel injury. *Circ Res* **105**, 965, 2009.
64. Rudolph, T.K., Rudolph, V., Edreira, M.M., *et al.* Nitro-fatty acids reduce atherosclerosis in apolipoprotein E-deficient mice. *Arterioscler Thromb Vasc Biol* **30**, 938, 2010.
65. Ambrozova, G., Martiskova, H., Koudelka, A., *et al.* Nitro-oleic acid modulates classical and regulatory activation of macrophages and their involvement in pro-fibrotic responses. *Free Radic Biol Med* **90**, 252, 2016.
66. Rudolph, T.K., Ravekes, T., Klinke, A., *et al.* Nitrated fatty acids suppress angiotensin II-mediated fibrotic remodelling and atrial fibrillation. *Cardiovasc Res* **109**, 174, 2016.
67. Florczyk, U., Jazwa, A., Maleszewska, M., *et al.* Nrf2 regulates angiogenesis: effect on endothelial cells, bone marrow-derived proangiogenic cells and hind limb ischemia. *Antioxid Redox Signal* **20**, 1693, 2014.

Address correspondence to:

William R. Wagner, PhD

Departments of Bioengineering and Surgery

McGowan Institute for Regenerative Medicine

University of Pittsburgh

Bridgeside Point Building II

450 Technology Drive, Suite 300

Pittsburgh PA 15219

E-mail: wagnerwr@upmc.edu

Received: August 8, 2017

Accepted: November 14, 2017

Online Publication Date: February 28, 2018